Computers and Fluids 220 (2021) 104883

Contents lists available at ScienceDirect

Computers and Fluids

journal homepage: www.elsevier.com/locate/compfluid

Simulation of a bubble rising at high Reynolds number with mass-conserving finite element lattice Boltzmann method

Lina Baroudi[a], Taehun Lee[b,*]

[a] Department of Mechanical Engineering, Manhattan College, Bronx, NY 10471, USA
[b] Department of Mechanical Engineering, City College of New York, New York, NY 10031, USA

ARTICLE INFO

Article history:
Received 3 June 2020
Revised 31 January 2021
Accepted 12 February 2021
Available online 23 February 2021

Keywords:
Lattice Boltzmann method
Finite element method
Bubble dynamics
High Reynolds number
Conservative phase-field
Bubble lateral motion

ABSTRACT

A mass-conserving finite element lattice Boltzmann equation (FE-LBE) method for the simulation of a bubble rising in viscous fluid at high Reynolds number with large material property contrast is presented in this work. The presented model consists of the conservative phase-field equation for interface capturing and the pressure-velocity formulation of lattice Boltzmann equation (LBE) for recovering the hydrodynamic properties. In this computational framework, LBE is regarded as a special space time discretization of the discrete Boltzmann equation in the characteristic direction and the streaming step is carried out by solving a linear advection equation in an Eulerian framework. We conduct extensive investigations for numerical accuracy and stability through performing multiple benchmark simulations for single bubble rising in a viscous fluid in different flow regimes. The complex dynamics of a high Reynolds number bubble rising with path and shape oscillations are studied and compared to available experimental results. The simulated evolution of the bubble mean shape with Archimedes number, path and shape oscillations in different oscillation regimes, and wake dynamics of the bubble show a good agreement with available experimental data. The current model offers a remarkable improvement in mass conservation compared to the Cahn-Hilliard based FE-LBE model.

1. Introduction

When two fluids are in contact, the interface formed between them often plays a central role in the dynamics of the involved physical processes. In general, the mathematical treatment of such a system is complicated by the fact that the position of the interface is not known a priori. Rather it evolves according to the flow within both fluid components. Methods for solving moving-interface problems fall into two broad categories: interface tracking and interface capturing [1,2]. Interface tracking approach uses a moving mesh with grid points residing on the interface. On the other hand, interface capturing approach determines the position of the interface by using a scalar function, whose evolution is typically represented by an advection equation on a fixed grid. Theoretically, both treat the interface as a zero-thickness surface, though an essential ingredient in the fixed-grid methods is a numerical regularization that spreads the interfacial force over a volume. In recent years, the phase-field model has gained popularity in simulating two-phase flows of complex fluids. This model differs from other fixed-grid methods in that the interface is diffuse in a physical rather than numerical sense [3–5]. The diffuse interface is introduced through an energetic variational procedure that results in a thermodynamic consistent coupling system. The interfacial region is represented by continuous variations of a phase-field variable in a way consistent with microscopic theories of the interface [6]. The interfacial position and thickness are determined by the phase-field variable whose evolution is governed by a mixing energy according to either Allen-Cahn [7] or Cahn-Hilliard [8] types of dynamics. This way, the structure of the interface is rooted in molecular forces; the tendencies for mixing and demixing are balanced through the nonlocal mixing energy. This distinguishes the phase-field method from other fixed-grid methods such as level set and volume-of-fluid, where the interface is sharp conceptually but regularized numerically by spreading the interfacial force over a volume. The significance of this physical root is essential for problems that involve topological transitions, i.e. bearkup and coalescence, contact line dynamics, and complex rheology.

The lattice Boltzmann method (LBM) has been demonstrated to be an effective computational tool for simulating multi-phase flows and interfacial flow phenomena. The conventional lattice Boltzmann equation (LBE) method compromises collison and streaming steps. The streaming of the particle distribution function is given

* Corresponding author.
E-mail addresses: lina.baroudi@manhattan.edu (L. Baroudi), thlee@ccny.cuny.edu (T. Lee).

https://doi.org/10.1016/j.compfluid.2021.104883
0045-7930/

as the exact solution of linear advection equation so that it offers exact numerical solutions. Severe limitations arise, however, from the use of uniform cartesian grids and its inherent instability at high Reynolds number (Re). These two aspects are closely related to each other in that LBE is a discretized form of the discrete Boltzmann equation (DBE) along characteristics, and thus the time and space discretizations are strongly coupled. Since He et al. [9] and Abe [10] showed that the discretization of physical space does not necessarily need to couple with the discretization of momentum space, several efforts have been devoted to address the treatment of curved or irregular boundaries and the control of mesh resolution at desirable regions, and significant progress has been achieved in recent years to overcome the limitations of LBM. Various numerical methods have been applied directly to the discrete Boltzmann equation (DBE) using finite difference (FD) [11–16], finite volume (FV) [17–19], finite element (FE) [20–23], and spectral-element discontinuous Galerkin (SEDG) methods [24,25]. The lattice Boltzmann method with Galerkin finite element discretization (FE-LBE) proposed by Lee and Lin [20,21] to simulate incompressible flows on unstructured mesh has been successfully applied to variety of flow phenomena [20–22]. This model provides geometrical flexibility and enables the use of an unstructured mesh to increase numerical accuracy while reducing computational cost.

Most of the existing multi-phase LBE models [26–28] are based on the Cahn-Hilliard (CH) theory [6,8]. Although Cahn-Hilliard dynamics conserve the mass over the entire domain, the enclosed area obtained by its interface is not preserved. It has been shown that CH equation causes small enclosed mass such as drops or bubbles to disappear once their radius is below a critical value [29,30]. Another downside of the Cahn-Hilliard equation is the calculation of the fourth-order spatial derivatives term which causes numerical complications. On the other hand, the Allen-Cahn equation [7] only requires second-order derivatives and is easier to handle numerically, but does not automatically ensure conservation of mass. Sun and Beckermann [31] proposed a conservative phase-field equation based on the Allan-Cahn equation that has been reformulated in a conservative from by Chiu and Lin [32]. The conservative phase-field equation conserves mass and requires only second-order derivatives. A derivative-free LBE formulation of the conservative phase-field equation is presented by Geier et al. [33].

In this work, we will combine the conservative phase-field equation for interface capturing and the pressure-velocity formulation of LBE similarly to [27,34] to propose a mass conserving LB model for the simulation of two-phase flow at higher Reynolds numbers with large material property contrast. As a diffuse interface method, phase interface of FE-LBE method is spread over several elements, and interface tension is transformed into volumetric force, which is governed by thermodynamic equilibrium of the free energy. To assess the accuracy and stability of the proposed model, extensive numerical investigations are carried out to study rising bubble problems.

2. Numerical methods

2.1. Conservative phase field equation

The conservative phase field equation for tracking the interface in the incompressible two-phase flow is given by [32]

$$\frac{\partial \phi}{\partial t} + u_j \frac{\partial \phi}{\partial x_j} = \frac{\partial}{\partial x_j}\left(M(\phi) \frac{\partial \phi}{\partial x_j} \right), \tag{1}$$

where ϕ is the phase-field variable that indicates each phase, u_j is the macroscopic velocity, $M(\phi) = \tilde{M}\left(1 - \frac{4\phi(1-\phi)}{\xi}\frac{1}{|\nabla\phi|}\right)$ is the mobility, and ξ is the interface thickness. $\tilde{M}$ is the tunable mobility parameter that determines how fast the interface reaches equilibrium profile and it's value is chosen based on numerical accuracy and stability. The phase indicator takes on values of $\phi_l = 0$ and $\phi_h = 1$ in the bulk of the light and heavy fluids, respectively. At equilibrium, the phase field variable along the direction normal to the interface assumes a hyperbolic tangent profile

$$\phi = \frac{1}{2} + \frac{1}{2}\tanh\left(\frac{2z}{\xi}\right), \tag{2}$$

where z is the spatial variable normal to the interface located at $z = 0$. In this case $4\phi(1-\phi)/\xi = \partial\phi/\partial\mathbf{n} = |\nabla\phi|$ with $\mathbf{n}$ being the unit interface normal vector, holds.

We apply the explicit Taylor-Galerkin finite element method to solve Eq. (1). The Taylor-Galerkin approximation of Eq. (1) yields

$$\begin{aligned}\phi^{n+1} = \phi^n - \delta t\left[u_j^n \frac{\partial \phi^n}{\partial x_j} - \frac{\partial}{\partial x_j}\left(M(\phi^n)\frac{\partial \phi^n}{\partial x_j}\right)\right] \\ + \frac{\delta t^2}{2} u_i^n \frac{\partial}{\partial x_i}\left(u_j^n \frac{\partial \phi^n}{\partial x_j}\right),\end{aligned} \tag{3}$$

where δt is the time step and the superscripts $(\cdot)^{n+1}$ and $(\cdot)^n$ denote (t) and $(t-\delta t)$, respectively. The domain Ω is discretized into an appropriate collection of finite elements. The Galerkin approximation is then used to find an approximate solution of the following form in a finite dimensional subspace H^h of the Sobolev space on the spatial domain Ω, $\phi = \mathbf{N^T}\vec{\phi}$, where $\mathbf{N^T} = N^1, N^2, \ldots, N^{n_e}$ is a $(1 \times n_e)$ vector of interpolation functions of the element Ω^e, the superscript $(\cdot)^T$ denotes the transpose operation, and n_e is the number of nodal points in an element. $\vec{\phi}$ is a $(n_e \times 1)$ vector of nodal phase-field variable. The weak form of Eq. (3) is derived by multiplying it with the weight function and integrating over the spatial domain of the problem. We then perform integration by parts on the terms introduced by Galerkin procedure and apply divergence theorem. The weak form of Eq. (3) is

$$\begin{aligned}&\int_{\Omega^e} \mathbf{N}\left(\phi^{n+1} - \phi^n\right) d\Omega \\ &= -\delta t\left[\int_{\Omega^e} \mathbf{N} u_j^n \frac{\partial \phi^n}{\partial x_j} d\Omega + \int_{\Omega^e} \frac{\partial \mathbf{N}}{\partial x_j}\left(M(\phi^n)\frac{\partial \phi^n}{\partial x_j}\right) d\Omega\right] \\ &\quad - \frac{\delta t^2}{2}\left[\int_{\Omega^e} \frac{\partial \mathbf{N}}{\partial x_i} u_i^n u_j^n \frac{\partial \phi^n}{\partial x_j} d\Omega\right],\end{aligned} \tag{4}$$

where the surface integrals due to integration by parts are assumed to be zero. The mass matrix in Eq. (4) is symmetric positive definite and can be solved by the Conjugate Gradient method using the solution from the previous time step as an initial guess. The density and phase-field variable are related linearly by $\rho = \rho_h\phi + \rho_l(1-\phi)$, where ρ_h and ρ_l are the bulk densities of the heavy and light fluids, respectively. The time step is restricted by the Courant-Friedrichs-Lewy condition $CFL \leq 1/\sqrt{3}$ [35,36], where $CFL = |e_\alpha|\delta t/dx$, $e\alpha$ is the microscopic particle velocity. We set $CFL = 0.2$ or 0.3 in our simulations which results in a sufficiently small time step that guarantees accuracy and stability.

2.2. Velocity-pressure latticeBoltzmann equation

The discrete Boltzmann equation for the velocity-pressure formulation can be written as

$$\frac{\partial f_\alpha}{\partial t} + e_{\alpha i}\frac{\partial f_\alpha}{\partial x_i} = -\frac{1}{\lambda}\left(f_\alpha - f_\alpha^{eq}\right) + F_\alpha, \tag{5}$$

where f_α is the particle distribution function for pressure and velocity along α direction, $e_{\alpha i}$ is the microscopic particle velocity, and λ is the relaxation time, and the equilibrium distribution function

is given by

$$f_\alpha^{eq} = t_\alpha\left[\bar{p} + e_{\alpha i}u_i + \frac{(e_{\alpha i}u_i)^2}{2c_s^2} - \frac{u_i u_i}{2}\right], \tag{6}$$

where t_α is a weighting factor, c_s is the lattice speed of sound, $\bar{p} = p/\rho$ with p being the dynamic pressure. F_α is a collection of forcing terms

$$\begin{aligned} F_\alpha = &-\Gamma_\alpha(e_{\alpha i}-u_i)\left(\frac{1}{\rho}\frac{\partial p}{\partial x_i}\right) + \Gamma_\alpha(0)(e_{\alpha i}-u_i)\left(\frac{\partial \overline{p}}{\partial x_i}\right) \\ &+\Gamma_\alpha(e_{\alpha i}-u_i)\left[\frac{\mu}{\rho}\nabla\phi + \frac{\eta}{\rho^2}\left(\frac{\partial u_i}{\partial x_j}+\frac{\partial u_j}{\partial x_i}\right)\frac{\partial \rho}{\partial x_j} + \frac{1}{\rho}G_i\right], \end{aligned} \tag{7}$$

in which

$$\Gamma_\alpha(u_i) = t_\alpha\left[1 + \frac{e_{\alpha i}u_i}{c_s^2} + \frac{(e_{\alpha i}u_i)^2}{2c_s^4} - \frac{u_i u_i}{2c_s^2}\right]. \tag{8}$$

In Eq. (7), $\mu = 4\beta(\phi-\phi_h)(\phi-\phi_l)(\phi-\frac{1}{2}) - \kappa\nabla^2\phi$ is the chemical potential for binary fluids. The coefficients β and κ are related to the surface tension σ and interface thickness ξ by $\beta = 12\sigma/\xi$ and $\kappa = 3\sigma\xi/2$, η is the dynamic viscosity that is determined from the relaxation time by $\eta = c_s^2\rho\lambda\delta t$, and G_i is the buoyant force acting on the bubble.

The recovered pressure evolution and velocity equations are

$$\frac{\partial \bar{p}}{\partial t} + u_i\frac{\partial \bar{p}}{\partial x_i} + c_s^2\frac{\partial u_i}{\partial x_i} = 0, \tag{9}$$

$$\begin{aligned} &\frac{\partial u_i}{\partial t} + \frac{\partial u_i u_j}{\partial x_j} = -\frac{1}{\rho}\frac{\partial p}{\partial x_i} + \frac{\mu}{\rho}\nabla\phi \\ &+\frac{1}{\rho}\frac{\partial}{\partial x_j}\left[\eta\left(\frac{\partial u_i}{\partial x_j}+\frac{\partial u_j}{\partial x_i}\right)\right] + \frac{1}{\rho}G_i. \end{aligned} \tag{10}$$

The above system of equations are the nearly incompressible Navier-Stokes equations with the fluid speed of sound c_s in the bulk phases and the interfacial region.

Eq. (5) is solved in two sequential steps at a nodal point ($\mathbf{x}$) [21]:

Collision step

$$f_\alpha(\mathbf{x}, t-\delta t) := f_\alpha(\mathbf{x}, t-\delta t) - \frac{1}{\tau+0.5}\left(f_\alpha - f_\alpha^{eq}\right)|_{(\mathbf{x},t-\delta t)}, \tag{11}$$

Streaming step with forcing term

$$f_\alpha^{n+1} = f_\alpha^n - \delta t\left(e_{\alpha i}\frac{\partial f_\alpha^n}{\partial x_i} - F_\alpha^n\right) + \frac{\delta t^2}{2}e_{\alpha j}\frac{\partial}{\partial x_j}\left(e_{\alpha i}\frac{\partial f_\alpha^n}{\partial x_i} - F_\alpha^n\right), \tag{12}$$

where $\tau = \lambda/\delta t$ is the nondimensional relaxation time. When taking moments, the distribution functions recover the macroscopic variables

$$\begin{aligned} &\sum_{\alpha=0} f_\alpha = \bar{p}, \\ &\sum_{\alpha=0} e_{\alpha i}f_\alpha = u_i c_s^2, \end{aligned} \tag{13}$$

We now apply the standard Galerkin finite element method to the streaming step. The domain Ω is discretized into an appropriate collection of finite elements. The Galerkin approximation is then used to find an approximate solution of the following form in a finite dimensional subspace H^h of the Sobolev space on the spatial domain Ω:

$$f_\alpha = \mathbf{N}^T\mathbf{f}_\alpha, \tag{14}$$

where $\mathbf{N}^T = \{N^1, N^2, \ldots, N^{n_e}\}$ is a $(1\times n_e)$ vector of interpolation functions of the element Ω^e, the superscript $(\cdot)^T$ denotes the transpose operation, and n_e is the number of nodal points in an element. $\mathbf{f}_\alpha$ is a $(n_e\times 1)$ vector of redefined nodal particle distribution functions. The other variables are expressed in the identical manner.

The weak form of Eq. (12) is

$$\begin{aligned} &\int_{\Omega^e}\mathbf{N}\left(f_\alpha^{n+1} - f_\alpha^n\right)d\Omega \\ &= -\delta t\left[\int_{\Omega^e}\mathbf{N}e_{\alpha i}\frac{\partial f_\alpha^n}{\partial x_i}d\Omega - \int_{\Omega^e}\mathbf{N}F_\alpha^n d\Omega\right] \\ &\quad -\frac{\delta t^2}{2}\left[\int_{\Omega^e}\frac{\partial \mathbf{N}}{\partial x_j}e_{\alpha j}e_{\alpha i}\frac{\partial f_\alpha^n}{\partial x_i}d\Omega - \int_{\Omega^e}\frac{\partial \mathbf{N}}{\partial x_j}e_{\alpha j}F_\alpha^n d\Omega\right] \end{aligned} \tag{15}$$

As before, the surface integrals due to integration by parts are assumed to be zero. The dimensionless relaxation time is taken as linear functions of the phase-field variable $\tau(\phi) = \phi\tau_h + (1-\phi)\tau_l$.

3. Numerical validation

In order to assess the presented mass-conserving FE-LBE model several benchmark studies with material property contrast are considered. A single bubble rising in different flow regimes is first simulated. Next, the mass conservation property of the proposed FE-LBE model is verified and a convergence study is conducted. Then, the dynamics of a high Reynolds number two dimensional bubble are investigated using the present model. Unless otherwise stated, we utilize the D2Q9 lattice structure [37] for the two dimensional (2D) problems presented in this section.

3.1. Single bubble rising in different shape regimes

A bubble rising and deforming under the influence of gravitational force is one of the very fundamental examples of multiphase flows.The understanding of the bubble rising physics is essential for the design and operation of industrial applications such as gas-liquid column reactors. The dynamic behavior of a rising bubble has been a subject of both experimental and numerical studies for many years. Experimental studies and correlations were reviewed by Clift et al. [38]. Rising of a bubble in a viscous fluid under the influence of gravitational forces can be generally grouped in three different regimes: Spherical, ellipsoidal, and spherical cap [38]. These regimes are achieved, depending on the values of Bond number (Bo) and Morton number (Mo) defined as:

$$Bo = \frac{g\rho_h d^2}{\sigma}, \tag{16}$$

$$Mo = \frac{g\eta_h^4}{\sigma^3\rho_h}, \tag{17}$$

where g is the gravitational acceleration in the vertical direction, ρ_h is liquid density, d is the initial bubble diameter, σ is the surface tension, η_h is liquid viscosity. Bo is the ratio of the gravitational forces and the surface tension. Mo provides a description of the properties of the surrounding fluid, mainly focusing on viscosity and surface tension. Based on experimental data on the motion of air bubbles in liquids, Grace et al. [39] constructed a diagram (Fig. 2 in [39]) that describes how the bubble behavior depends on Bo, Mo, and terminal Reynolds number defined as $Re = \frac{\rho_h U_t d}{\eta_h}$, where U_t is the terminal velocity of the bubble. Terminal velocity is defined as the steady velocity that the bubble reaches when there is a balance between buoyancy and drag forces. A general classification of the bubble is usually done depending on the final shape or by the primary forces acting on the system. However, the transition areas from regime to regime are still not well defined.

In this study, two dimensional (2D) numerical simulations were performed using the mass-conserving FE-LBE model to simulate

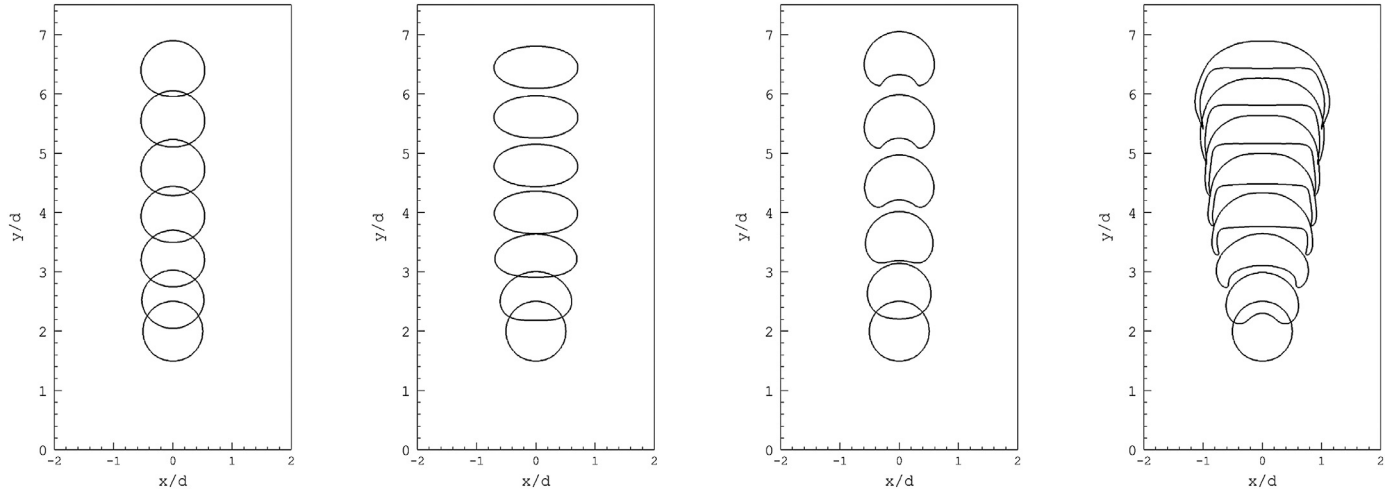

Fig. 1. Shape and position evolution for cases A, B, C, and D from left to right, respectively.

four cases corresponding to steady regimes in the shape regime map [39] with different final bubble shape. The parameters and results, in terms of *Bo*, *Mo*, terminal *Re*, and final bubble shapes are listed in Table 1. The column under Re_G lists terminal Reynolds numbers extracted from the Grace diagram. The Simulations were performed in a 2D computational domain of the size $9d \times 18d$ and resolution 450×900. Periodic boundary condition is imposed in the vertical direction and the no slip boundary condition is applied at the left and right walls. The viscosity and density ratios are, $\eta_h/\eta_l = 100$, and $\rho_h/\rho_l = 100$, respectively. The nondimensional measure for the interface thickness is the Cahn number, defined by $Cn = \xi/d$ and has a value of 0.05 in all simulations presented in this section.

For the parameters considered in this section, the bubble ascends in a rectilinear path and the shape development of the two dimensional bubbles is expected to follow well the experimental results in the absence of three dimensional effects such as wobbly motion of the bubble. The similarity between the 2D simulations and the experimental results as well as three dimensional simulations has been established by Chen et al. [40] and observed in previous numerical simulations [41,42]. Fig. 1 shows the shape and position evolution of the bubbles in different regimes. The observed bubble shapes are in agreement with the shape regime diagram presented in Fig. 2 in Ref. [39] and the agreement of computed *Re* and Re_G is satisfactory.

3.2. Mass conservation

One of the key features of the proposed conservative phase-field FE-LBE is that it preserves the area enclosed by an interface better than Cahn-Hilliard based models. The mass enclosed by the interface of a rising bubble is checked for a bubble rising in the spherical regime, as in case A (see Table 1) presented in the pervious section, to verify the mass conservation property of the model. The simulation was performed in a (2D) computational domain of the size $10d \times 10d$ and resolution 250×250. Periodic boundary condition is imposed in the vertical direction and the no slip boundary condition is applied at the left and right walls. The viscosity and density ratios and Cahn number are, $\eta_h/\eta_l = 100$, $\rho_h/\rho_l = 100$, and $Cn = 0.1$, respectively. The results of the current model are compared with the FE-LBE model based on Cahn Hilliard equation [22]. The enclosed mass M is normalized by the initial enclosed mass M_0 of the bubble, and its evolution is plotted versus dimensionless time $T = t\sqrt{\frac{g}{d}}$ in Fig. 2. As can be seen in Fig. 2, the mass enclosed by the bubble's interface is gradually decreasing in the Cahn Hilliard based FE-LBE model, while the current model preserves the enclosed mass (Fig. 2).

Table 1
Parameters of the simulated cases for single bubble rising in different shape regimes. *Re* is the computed terminal Reynolds number, and Re_G is experimental data extracted from Fig. 2 in [39].

Case	Bo	Mo	Re	Re_G	Bubble shape
A	10	100	0.21	0.17	Spherical
B	10	0.01	9.9	11	Oblate
C	100	1000	1.34	1.6	Ellipsoidal cap, dimpled
D	100	1	18	19	Ellipsoidal cap, skirted

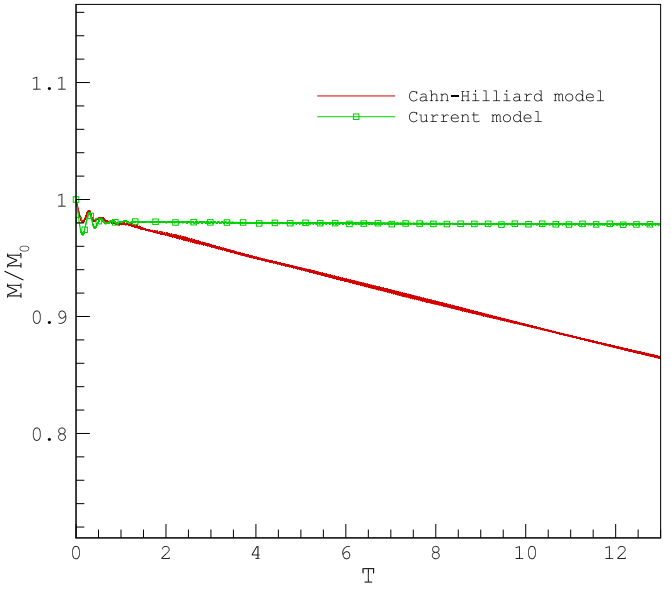

Fig. 2. Variation of the mass of enclosed area by the bubble interface versus time. The red line shows the results of the Cahn Hilliard based model and the green line with square symbols shows the results of the conservative phase field based model. (For interpretation of the references to colour in this figure legend, the reader is referred to the web version of this article.)

3.3. Convergence study

To assess the convergence of the proposed mass-conserving FE-LBE model, we consider the rise of a two dimensional bubble due to buoyancy force according to the well established benchmark

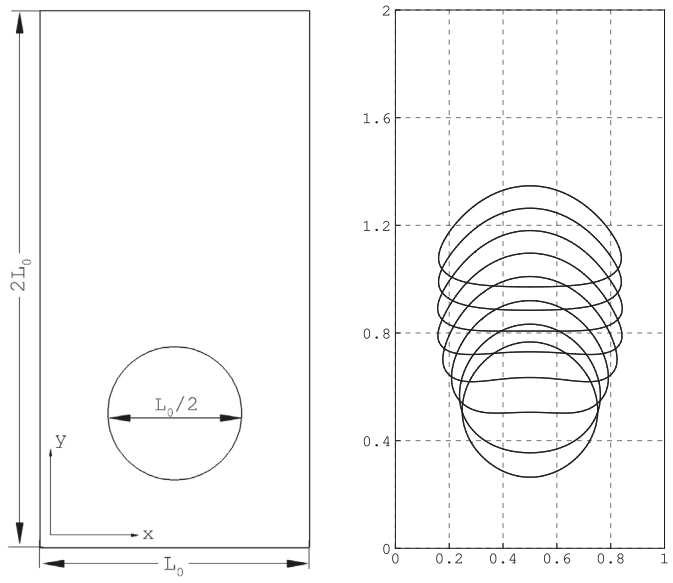

Fig. 3. (a) Initial configuration for the rising bubble problem [43]. (b) The evolution of the bubble shape at equally spaced time intervals.

proposed by Hysing et al. [43]. Initially, a circular bubble with an initial diameter $d = L_0/2$ is placed at $(L_0/2, L_0/2)$ in a rectangular domain of length $2L_0$ and width L_0 as illustrated in Fig. 3(a), where $L_0 = 1$. The no slip boundary condition is applied at the top and bottom walls, while periodic boundary conditions are used at the lateral boundaries, which is identical, in this particular case, to the slip boundary condition used in [43]. The bubble is allowed to rise due to the buoyancy force $\mathbf{G} = -\mathbf{g}(\rho - \rho_h)$. The characteristic dimensionless numbers are Bond and Archimedes numbers. The Archimedes number is defined as:

$$Ar = \frac{\rho_h \sqrt{\mathbf{g} d^3}}{\mu_h}. \tag{18}$$

The parameters for the studied test cases are taken from Hysing et al. [43]. The simulations were started with a reduced Ar, which was ramped up successively to the desired Ar to avoid initial velocity oscillations due to the weak compressibility effects inherited in the (nearly) incompressible LBM. In order to have consistent measurements with [43], the following equation is used to calculate the macroscopic time, $T = t\sqrt{\frac{g}{g_0}}$, where $g_0 = 0.98$ is the macroscopic gravity used in [43]. The mean rise velocity of the bubble and its centroid are calculated as:

$$\mathbf{U}_c = \frac{\int_{\Omega_l} \mathbf{u} dx}{\int_{\Omega_l} 1 dx} \tag{19}$$

$$\mathbf{X}_c = \frac{\int_{\Omega_l} \mathbf{x} dx}{\int_{\Omega_l} 1 dx}, \tag{20}$$

where Ω_l denotes the area inside the bubble. The circularity defined as the ratio of the of perimeter of area-equivalent circle and perimeter of the bubble P is given as:

$$C = \frac{\pi d}{P}$$

$$P = \int_{\Omega} |\nabla \phi| d\Omega \tag{21}$$

,where Ω is the area of the computational domain.

3.3.1. Test case 1

For the first test case, we consider the following parameters: $\rho_h/\rho_l = \mu_h/\mu_l = 10$, $Bo = 10$, and $Ar = 35$ as in [43]. With the given parameters, surface tension effects dominate the bubble shape and the bubble should belong to the ellipsoidal regime [39]. The interfacial thickness ξ is chosen proportional to grid size $1/h$, which keeps the number of elements along the interface fixed. Here, we have around three elements along the interface in all simulations. Fig. 3(b) shows the evolution of the bubble interface over time for a grid spacing of $h = 1/160$. The effect of the grid resolution on the bubble's shape at $T = 3$ of our simulation is shown in Fig. 4 for three different grid sizes of $1/h = 80, 160, 320$, along with the finite element solution of the FeatFlow software package in [43] with a grid spacing of $1/h = 320$. The FeatFlow results were slightly shifted for comparison purposes. We notice that the final shape resulting from each grid is almost overlapping each other and agrees well with the FeatFlow solution.

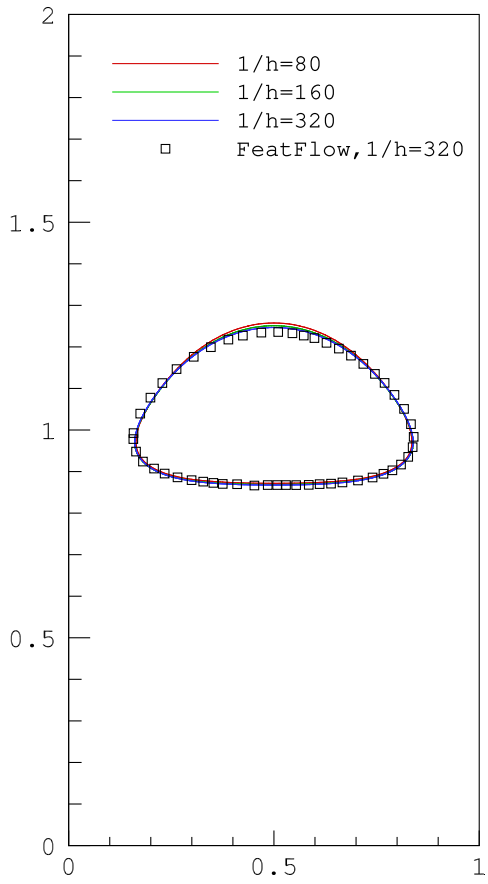

Fig. 4. Bubble interface shape at $T = 3$ for test case 1 on different grid levels.

Fig. 5 (a)–(c) show the convergence trend of the solution for the centroid position, the mean rising velocity of the bubble, and the circularity up to $T = 3.27$ along with the finite element solutions of FeatFlow with a grid spacing of $1/h = 320$. Since our simulations were started with a reduced Ar, which was ramped up to the desired Ar, the FeatFlow solutions have been slightly shifted by $T = 0.27$ for comparison purposes. As can be seen in Fig. 5(a)–(c), the centroid, mean rise velocity, and the circularity of the bubble converge nicely and show a good agreement with FeatFlow solution. Fig. 6 presents the convergence behaviour of the L_1, L_2 and L_∞ norm of errors in the rising velocity with reference to the solution from the computation on the finest grid spacing of $1/h = 640$. The error norms are defined

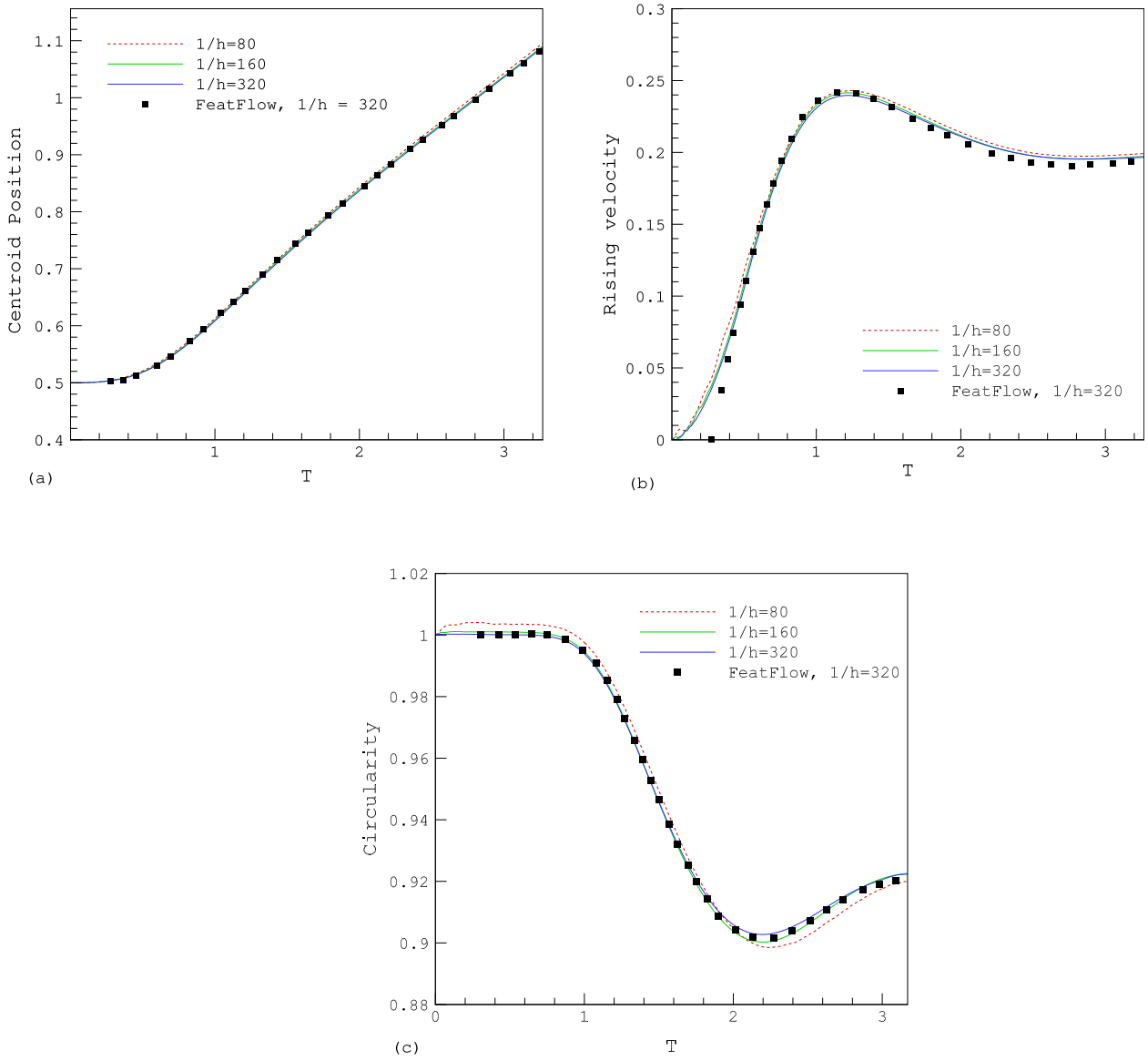

Fig. 5. Effect of grid resolution on the temporal evolution of the center of mass of the bubble (a), the bubble rising velocity (b), and circularity (c) on different grid levels.

as follows:

$$L_1\ error: \|e_1\| = \frac{\sum_{t=1}^{NTS} |q_{t,ref} - q_t|}{\sum_{t=1}^{NTS} |q_{t,ref}|}$$

$$L_2\ error: \|e_2\| = \left(\frac{\sum_{t=1}^{NTS} |q_{t,ref} - q_t|^2}{\sum_{t=1}^{NTS} |q_{t,ref}|^2} \right)^{1/2}$$

$$L_\infty\ error: \|e_\infty\| = \frac{max_t |q_{t,ref} - q_t|}{max_t |q_{t,ref}|},$$

where NTS is the number of sample points and q_t is the temporal evolution of the quantity q. The errors are calculated for grid spacing of $1/h = 80, 160, 320$. The convergence rates (ROC) for the quantities can be computed as

$$ROC = \frac{log_{10}(\|e^{(l-1)}\|/\|e^l\|)}{log_{10}(h^{(l-1)}/h^l)}, \tag{22}$$

where l is the grid refinement level. The relative error norms for the rise velocity are presented in Table 2 together with the estimated ROC. It is evident that the rising velocity converges with a more than linear convergence order.

3.3.2. Test case 2

The second test case is numerically more challenging as the density and viscosity ratios are increased to $\rho_h/\rho_l = 1,000$ and $\mu_h/\mu_l = 100$, respectively, with $Bo = 125$, and $Ar = 35$. With the given parameters, inertial effects take over the surface tension forces and the bubble exhibits pronounced deformation. This bubble belongs somewhere between the skirted and dimpled ellipsoidal-cap regimes [39]. Fig. 7 shows snapshots of the time evolution of the bubble computed on a grid spacing of $h = 1/160$. The decrease in surface tension compared to inertial forces causes this bubble to deform substantially and develops thin filaments. For this test case agreement between the numerical approaches

Table 2
Relative error norms and convergence orders for rise velocity in test case 1.

$1/h$	$\|e_1\|$	ROC_1	$\|e_2\|$	ROC_2	$\|e_\infty\|$	ROC_∞
80	2.08E-02		2.56E-02		6.12E-02	
160	8.90E-03	1.22	1.04E-02	1.31	2.06E-02	1.57
320	2.86E-03	1.64	3.15E-03	1.72	6.92E-03	1.57

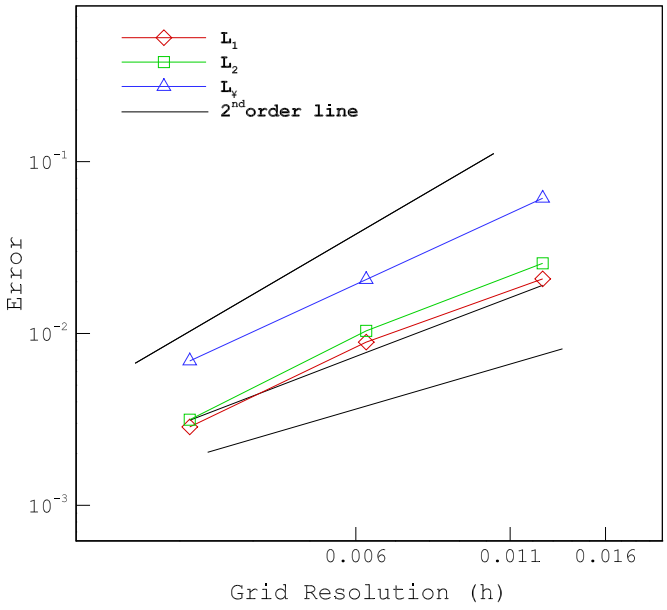

Fig. 6. Convergence behaviour for rising velocity in test case 1.

studied in [43] could not be achieved and only qualitative comparison with the results reported in [43] is considered here. Two of the three software packages utilized in [43] namely FeatFlow and FreeLIFE predicted filament break off. Alnad and Voigt [44] performed benchmark computations of three different diffuse interface models using the same parameters studied in [43]. For test case 2, none of the diffuse interface models considered in [44] yielded break off of the filament. It unclear if break off really should occur for this setting. The evolution of the bubble shape computed using the mass conserving FE-LBE model did not predict filament break up in agreement with [44]. The simulated bubble shape evolution shows a good qualitative agreement with the FeatFlow solution up to $T = 2.59$ before filament breakup [43].

4. Dynamics of a high Reynolds number bubble rising in viscous fluid

4.1. Background

Predicting the motion of bubbles in dispersed gas-liquid flows is a key problem in fluid mechanics that has a bearing on a wide range of applications such as bubble column, cooling systems in nuclear power plants and the transportation of the oil and natural gas in petroleum industry. In such applications, bubbles can induce a turbulent flow which requires modeling in predictive simulations. It is well established that a large bubble does not usually rise in a straight line but that its velocity and shape may oscillate due to the interaction between the bubble and its unsteady wake. The ascent characteristic of gas bubbles in liquid are strongly affected by their wakes. Due to the difficulty of measuring or simulating an oscillating bubble, most studies have focused on the average characteristics such as mean velocity and shape [45–47]. In recent years, the development of advanced measuring and simulation tools has enabled important progress in the investigation of the unsteady motion of bubbles rising in unbounded domain [48–51]. However, the detailed physical effects that determine the dynamics are not yet fully understood. The description and interpretation of bubble rise and deformation is still limited to a few flow regimes only, due to the difficulties in experiments, since it is not easy to measure, without any interference, the flow pattern and pressure distribution within a bubble and its surrounding liquid while it is rising and deforming. The study of the dynamics of bubbles in Hele-Shaw cells has been proposed as an effort to simplify the study of ascending bubbles by restricting the motion to one horizontal direction [52–59]. In this way, the available degrees of freedom are reduced since the description can be made in terms of the position and deformation in two spatial coordinates. For a bubble of apparent diameter d (as seen from the perpendicular direction of the plates) rising in a vertical Hele-Shaw cell of width h filled with a liquid at rest (Fig. 8), the non-dimensional numbers that control the dynamics are the confinement ratio h/d, the Archimedes number $Ar = \sqrt{gd}d/\nu_h$, Bond number $Bo = \rho_h g d^2/\sigma$, and the Reynolds number based on the vertical component of the bubble velocity $Re = U_t d/\nu_h$, where ν_h is the kinematic viscosity of the liquid. Based on the ratio of the magnitude of the inertial stress corresponding to the motion within the cell to that of the stress in the direction normal to the plates given as $Re(h/d)^2$, the studies of motion of bubbles in Hele-Shaw cell ($h/d \ll 1$) can be divided into two regimes:

- The classic Hele-Shaw regime: This regime corresponds to $Re(h/d)^2 \ll 1$ and $Re \gg 1$.
- The inertial regime: In this regime $Re(h/d)^2 \gg 1$ and $Re \gg 1$, and the in-plane flow is equivalent to high Re two dimensional flow.

Kelley and Wu [52] conducted experiments to study the instabilities of rising air bubbles using a tilted Hele-Shaw cell with a gap of 1.6 *mm*. They observed that the wake formed in the surrounding fluid due to the motion of the bubbles was similar to that observed behind solid cylinders and the onset of vortex shedding was found to be described as a supercritical bifurcation [52]. Beyond this transition, the bubbles followed a zigzag path due to the nonsymmetric pressure field at the surface generated by the vortex shedding. Roig et al. [54] conducted experiments using air bubbles in water moving in a cell with a gap between the plates of 1 *mm* and found a linear relationship between the Archimedes and terminal Reynolds numbers, namely $Re = 0.5Ar$.

Considering the difficulties in experimental investigations, numerical simulations provide an alternative means to investigate and attain a better insight into the bubble rising behavior, the development of bubble-shape evolution, and the induced flow in the surrounding liquid. Numerical studies of rising gas bubbles using various methods for the description of the phase interface have been performed [60]. Most of the numerical investigations of rising bubbles aim at model validation, for this reason in most cases the results are restricted to bubbles rising in a straight path at low to moderate Re [61–63]. Few numerical investigations of unsteady bubble wakes have been performed. In a recent work, Antepara et al. [64] conducted numerical simulations to study the dynamics of bubbles rising in the wobbling regime at moderate to high Reynolds numbers. Mougin and Magnaudet [50] performed numerical simulations to investigate the dynamics of unsteady bubble wakes with prescribed fixed bubble shapes. As in experiments, a pair of counter-rotating vortices were found in the wake of spiralling bubbles. For a bubble rising on a zigzag path the computed vertical vorticity indicates two vortices in the wake, which can be interpreted as the legs of a hairpin vortex. Gaudlitz et al. [65] studied the shape and path oscillation of a freely rising bubble in an unconfined domain at moderate Re and observed hairpin vortices in the wake of an initially zigzagging bubble. It should be noted that the vortex distribution around a bubble in a Hele-Shaw cell completely differs from the wake for an unconfined sphere or bubble formed by an elongated horseshoe vortex [66]. Wang et al. [57] studied numerically and experimentally the effect of confinement ratio on the bubble dynamics in a vertical Hele-Shaw cell. They found that the bubble shape and terminal velocity were influenced by the confinement ratio. Piedra et al. [56] investigated

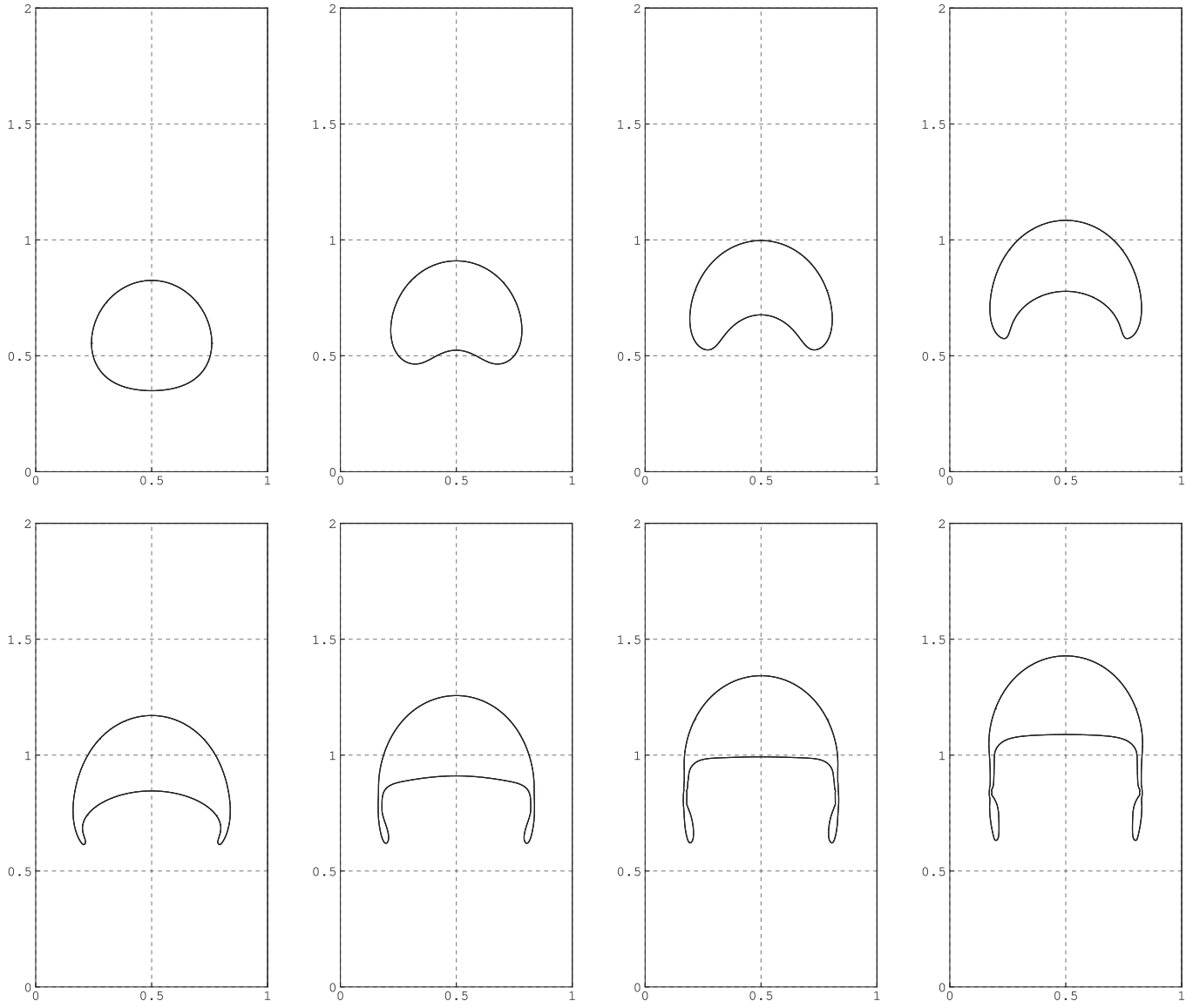

Fig. 7. Time evolution of the bubble shape in test case 2 for $1/h = 160$ at $T = 0.79$, $T = 1.15$, $T = 1.51$, $T = 1.87$, $T = 2.23$, $T = 2.59$, $T = 2.95$, and $T = 3.31$, from top to bottom and left to right.

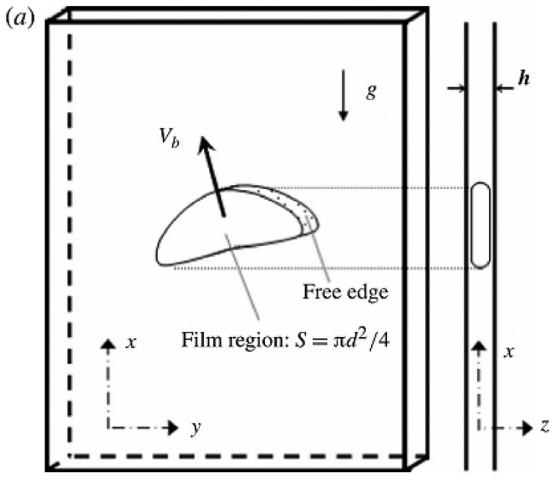

Fig. 8. A vertical Hele-Shaw cell for bubble dynamics studies. Adopted from Ref. [54].

the dynamics of two-dimensional bubbles ascending under the influence of buoyant forces numerically and experimentally. They observed that at high Reynolds numbers the two dimensional bubbles follow an approximately periodic zigzag trajectory and an unstable wake with properties similar to the Von Karman vortex street is formed.

4.2. Computational setup

In this study, we utilize the mass-conserving FE-LBE model to investigate the characteristics of the path and shape oscillations of two-dimensional bubbles rising at moderate and high *Re* in different regimes for a wide range of Archimedes number: $100 \leq Ar \leq 11,000$. Simulations were performed in a two dimensional computational domain of the size $22d \times 18d$ and resolution 1100×900. Periodic boundary condition is imposed in the ascent direction and no slip boundary condition is imposed in the horizontal direction. In all simulations presented in this section, the viscosity and density ratios, and Cahn number, are $\mu_h/\mu_l = 50$, $\rho_h/\rho_l = 50$, and $Cn = 0.05$, respectively. The values of *Ar* and *Bo* considered

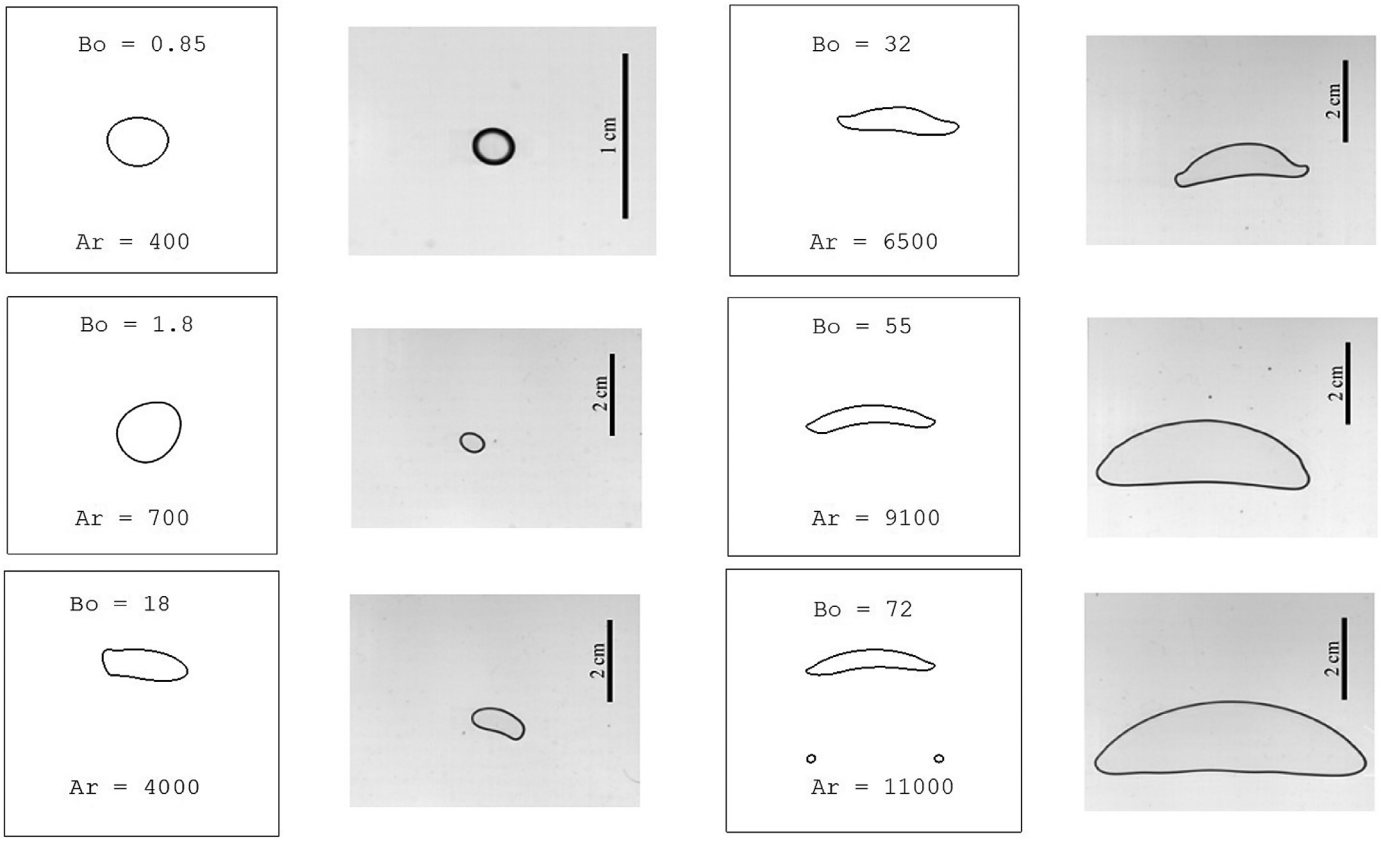

Fig. 9. Evolution of the bubble shape with *Ar* compared to the experimental results by Roig et al. [54] presented in the second and fourth columns.

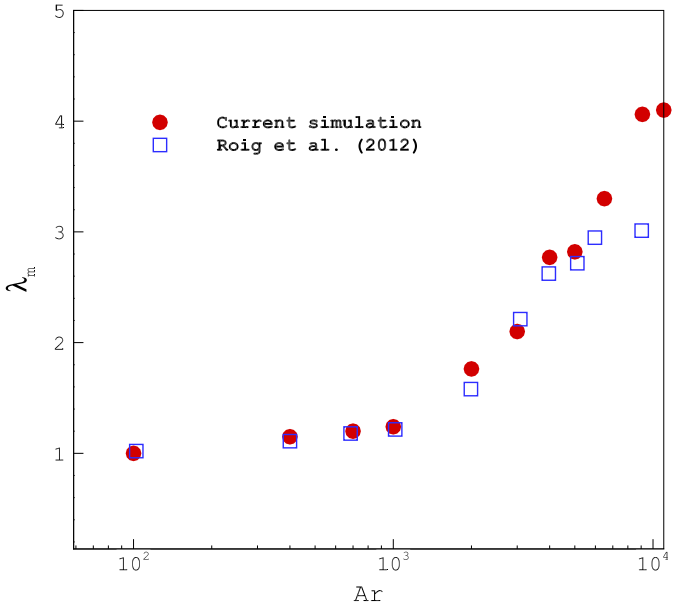

Fig. 10. (Color online) Comparison of the mean aspect ratio of the bubble at different Archimedes number with experimental results [54]. (For interpretation of the references to colour in this figure legend, the reader is referred to the web version of this article.)

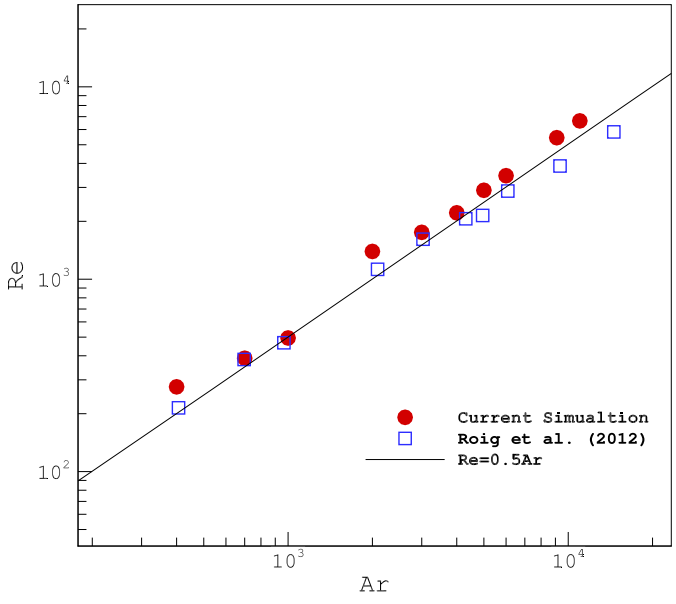

Fig. 11. (Color online) Terminal Reynolds number as a function of Archimedes number. The continuous line represents the scaling $Re = 0.5Ar$ observed by Roig et al. [54]. (For interpretation of the references to colour in this figure legend, the reader is referred to the web version of this article.)

in our simulations are (Ar, Bo): $(100, 0.14)$, $(400, 0.85)$, $(700, 1.8)$, $(1,000, 2.63)$, $(2,000, 7)$, $(3,000, 10)$, $(4,000, 18)$, $(5,000, 25.8)$, $(6,000, 30)$, $(6,500, 32)$, $(9,100, 55)$, $(11,000, 72)$. The results of our simulations are compared to the experimental results reported by Roig et al. [54] for a single bubble rising in a Hele-Shaw cell in the inertial regime.

For the simulation of rising bubbles the use of a computational domain with periodic boundary conditions in ascent direction allows for a computationally acceptable domain height. However, the bubble wake can have an effect over a significant distance up to $50d$ below the bubble as reported in the experimental findings

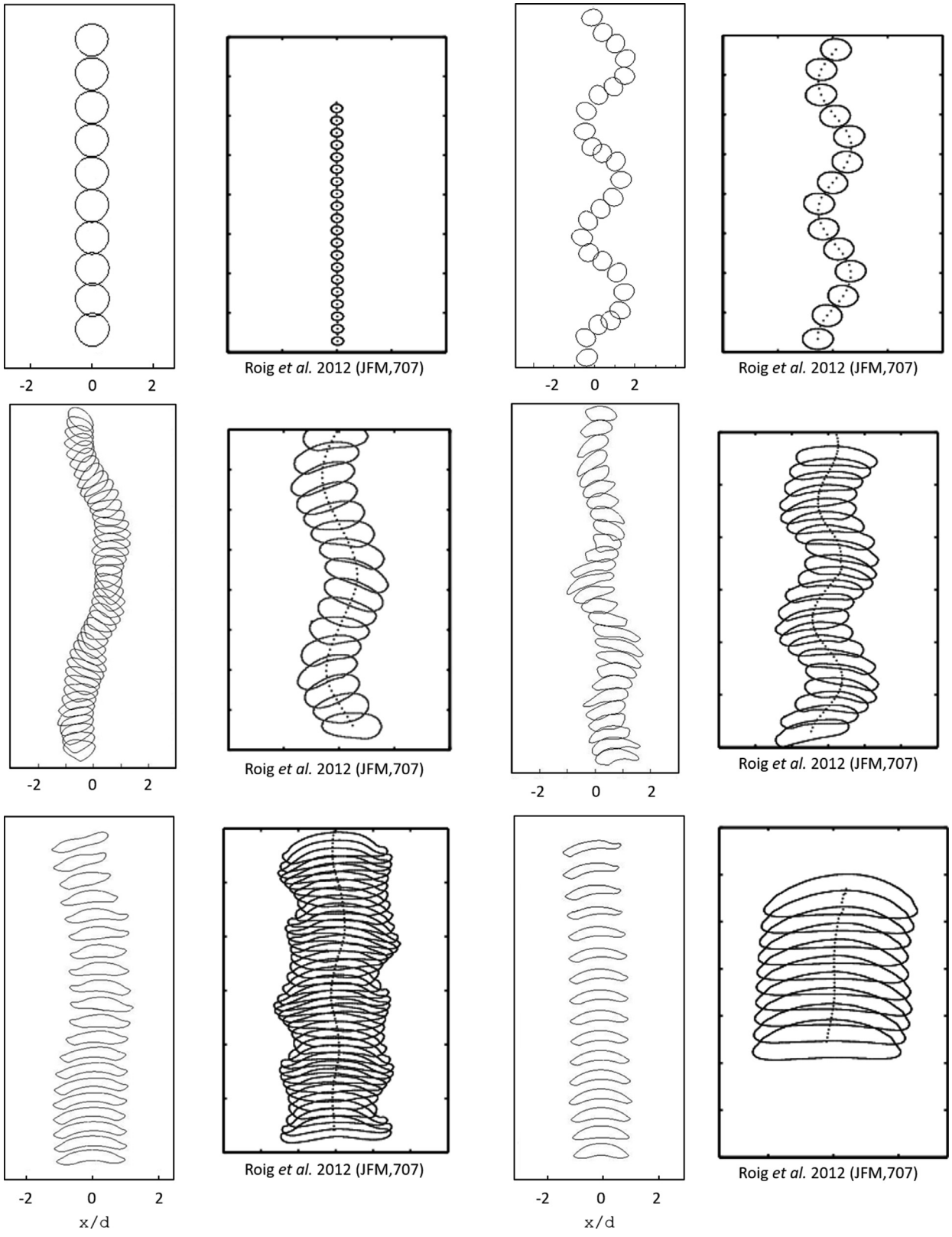

Fig. 12. Various regimes of shape and path oscillations compared to the experimental results of Roig et al. [54] at similar parameters. From left to right, top to bottom $Ar = 100$, $Ar = 700$, $Ar = 2,000$, $Ar = 4,000$, $Ar = 6,500$, $Ar = 9,100$.

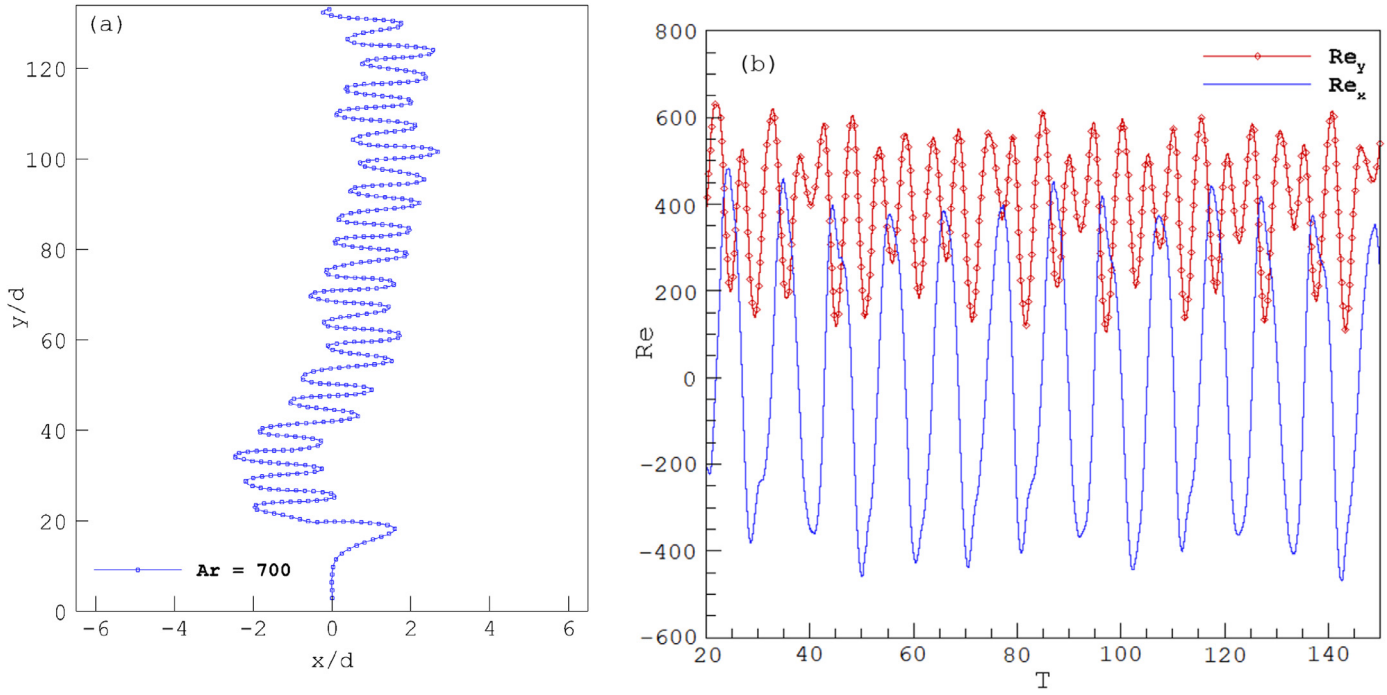

Fig. 13. (a) Trajectory of the centroid of an ascending bubble at $Bo = 1.8$ and $Ar = 700$; (b) horizontal and vertical Reynolds numbers as functions of the nondimensional time for $Bo = 1.8$ and $Ar = 700$.

by Ellingsen and Risso [49]. When using periodic computational domain the bubble might be affected by its own wake and the nonzero velocities ahead of the bubble originating from the bubble's wake can affect the shape and the dynamics of the bubble compare to a bubble rising in quiescent liquid. We utilize a fringe technique [65,67] in front of the rising bubble to suppress the velocities generated by the bubble's wake. Inside the fringe zone all the velocities are damped to zero. The fringe zone spans the entire horizontal plane and has a small height in the vertical direction $0.25d$. In order to maintain a constant distance from the bubble, the fringe zone is shifted with the bubble velocity U_t. The velocity inside the fringe zone are damped with the following forcing term $F_{fringe} = \frac{1}{\rho_h}\lambda(y)[U_0 - u(y)]$, toward a desired velocity U_0 (for our purpose $U_0 = 0$). The function $\lambda(y) = 0$ outside the fringe zone and takes the form of a smoothed step function inside the fringe zone as proposed by Schlatter et al. [67]. Details about the chosen fringe parameters are given in Appendix A.

4.3. Evolution of the bubble mean shape with Archimedes number

The evolution of the simulated bubble shape as a function of the Archimedes and Bond numbers is presented in Fig. 9 along with the experimental results from Roig et al. [54] at similar parameters. The deviation of the bubble from the circular shape is characterized by the mean aspect ratio λ_m of an ellipse equivalent to the bubble contour. Fig. 10 compares the change in the mean aspect ratio of the simulated bubble as function of Ar with experimental results. For $Ar < 600$ and $Bo < 1$, the bubble shape in this regime is dominated by surface tension and the bubble remains nearly circular with an aspect ratio close to unity. As Ar increases the aspect ratio of the bubble increases and the bubble becomes elongated and flattened and its mean shape is an ellipse. For $Ar > 4,000$, the bubble takes a more complex shapes and loses the fore-and-aft symmetry, as the rear of the bubble remains concave during its ascent on a periodic path. When $Ar > 6,500$ the bubble takes a circular capped shape and the aspect ratio of the bubble stops increasing anymore. The sequence of the two-dimensional bubble shapes is similar to that observed for bubbles free to evolve in a three-dimensional unconfined space. Overall, the evolution of bubble shape and it's mean aspect ratio show a good agreement with the experimental results reported by Roig et al. [54] for a wide range of Ar. For $Ar > 6,500$, the simulated bubble shape is more elongated and has a higher aspect ratio compared to the experimental data.

The change of Reynolds number Re with Ar in different shape regimes is compared to the experimental results at similar Ar and to the scaling law $Re = 0.5Ar$ observed by Roig et al. [54] in Fig. 11. For bubble rising with path and shape oscillations (see Section 4.4), the vertical velocity pulsates and average values of Re based on the vertical velocity component are reported in Fig. 11. We notice that the computed Reynolds number is proportional to the Archimedes number and shows a very good agreement with the linear scaling law proposed by Roig et al. [54]. However, some of the computed Re values are higher than the experimentally observed Re due to the drag force exerted by liquid films between the bubble and the cell walls as a result of possible interface contamination in the experiments.

4.4. Path and shape oscillations with Archimedes number

The simulated successive instantaneous bubble shapes along with their trajectories for different Ar in the range from $Ar = 100$ to 9,100 are presented in Fig. 12 with the experimental results of Roig et al. [54] at similar parameters. The oscillation frequency f of the ascending bubbles is characterized by the Strouhal number $St = 2\pi f d/U_t$. The experimental values of the Strouhal number St_{exp} are extracted from Fig. 14 in Roig et al. [54] at similar experimental conditions. For $Ar = 100$ the bubble rises in a rectilinear path ($St = 0$) and the shape of the bubble is nearly circular. At $Ar = 700$, a sinusoidal trajectory of the bubble can be observed and the bubble takes an ellipsoidal shape with negligible shape oscillations in agreement with experiment. The predicted value of the Strouhal number in this case $St = 1.07$ agrees well with the corresponding experimental value $St_{\text{exp}} \approx 1.01$. As Archimedes num-

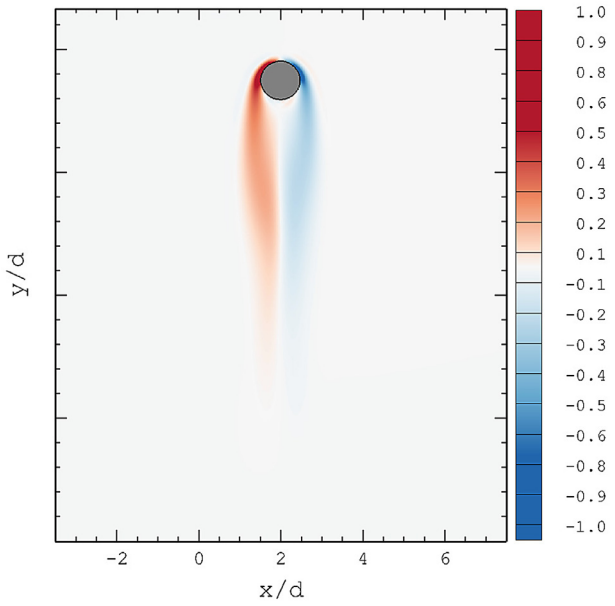

Fig. 14. Vorticity around the bubble at $Ar = 100$. Here and in the following similar figures, vorticity is normalized with respect to the maximum vorticity magnitude.

ber increases further $Ar \approx 2,000 - 6,500$, shape oscillations are added to the path oscillations. In this regime, the shape of the bubble is more elongated and the transverse elongation oscillates with a large amplitude. For $Ar = 2,000$, the bubble shape oscillates around an ellipse and the bubble has a zigzag path, with $St = 1.23$ which agree well with experiment $St_{\text{exp}} \approx 1.33$. At $Ar = 4,000$, the bubble follows a zigzag path with strong shape oscillations. The bubble oscillates with its rear part staying concave throughout the oscillation. The predicted oscillation frequency $St = 1.44$ for this case is slightly lower than the corresponding experimental value $St_{\text{exp}} \approx 1.65$. For $Ar = 6,500$, strong and complex shape oscillations are observed. At the front of the bubble, two moving regions of concave shape are always present and rear interface remains concave in agreement with experiment. The predicted path oscillation frequency $St = 1.66$ is slightly lower than the experimental value $St_{\text{exp}} \approx 1.98$ at similar conditions. For $Ar = 9,100$, the path and shape oscillations are strongly reduced. There still exist two points along the front interface where the curvature changes sign. At a higher $Ar > 9,100$, the bubble takes a circular cap shape and the path becomes rectilinear. The numerical results predict the path and shape oscillations properly and show a good agreement with the shape and path descriptions given by Roig el al. [54]. The predicted oscillation frequencies for $Ar > 2,000$ were found to be slightly lower than the corresponding experimental values. Our numerical simulations aim to give insights into bubble dynamics that approximate the motion of bubbles in the inertial Hele-Shaw regime.

For $Bo = 1.8$ and $Ar = 700$, the trajectory of the centroid of the bubble is shown in Fig. 13(a). The x and y axes are scaled with the bubble diameter d. Fig. 13(b) displays the instantaneous Reynolds numbers based on the horizontal Re_x and vertical Re_y velocity components as a function of the dimensionless time $T = t\sqrt{\frac{g}{d}}$ for $Bo = 1.8$ and $Ar = 700$. We notice a large oscillation of the horizontal component (Re_x) as a result of the zigzag motion of the bubble as seen in Figs. 12 and 13(a). The vertical motion also displays a small oscillation superposed on its average value. It can be seen from Fig. 13(b) that the frequency of the vertical velocity is twice that of the horizontal component with the maxima of the vertical velocity coinciding with the zeros of the horizonal velocity in agreement with the results obtained by Piedra et al. [56]. It is clear that the vertical velocity is not a simple harmonic and shows small variations in the amplitude due to the interaction of the bubble with the surrounding fluid.

4.5. Dynamics of the bubble wake

The simulated flow vorticity Ω_z is presented for different Ar in Figs. 14, 15, and 16 to give a better understanding of the coupling between the motion of the bubble, it's shape/path oscillations and the properties of its wake. For low Archimedes number, it can be seen from Fig. 14 that no vortex shedding is observed in the liquid, which means that the vorticity is not strong enough to form a vortex core, and the bubble has an attached, symmetrical wake without vortex shedding. Without the effect of vortex shedding, the path of the bubble is not perturbed and remains rectilinear. As Ar increases, the attached wake becomes unstable and detaches from the bubble, and vortex shedding is generated by the bubble as it rises (see Fig. 15) due to the fluid rotation around the

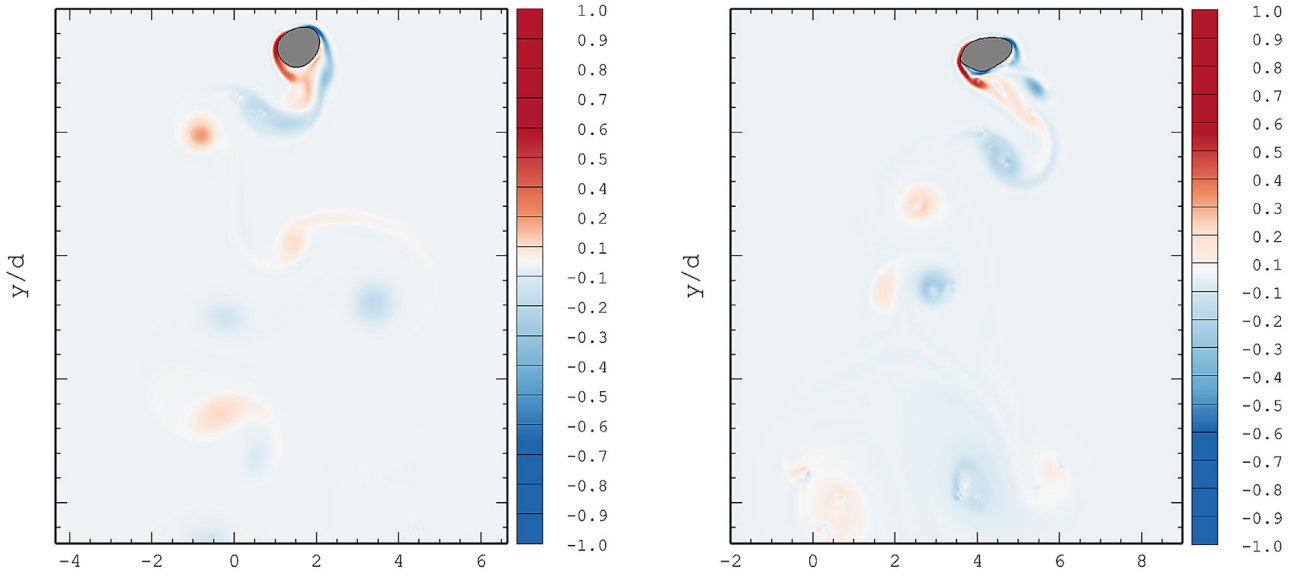

Fig. 15. Vorticity around the bubbles at $Ar = 700$ left panel and $Ar = 2000$ right panel.

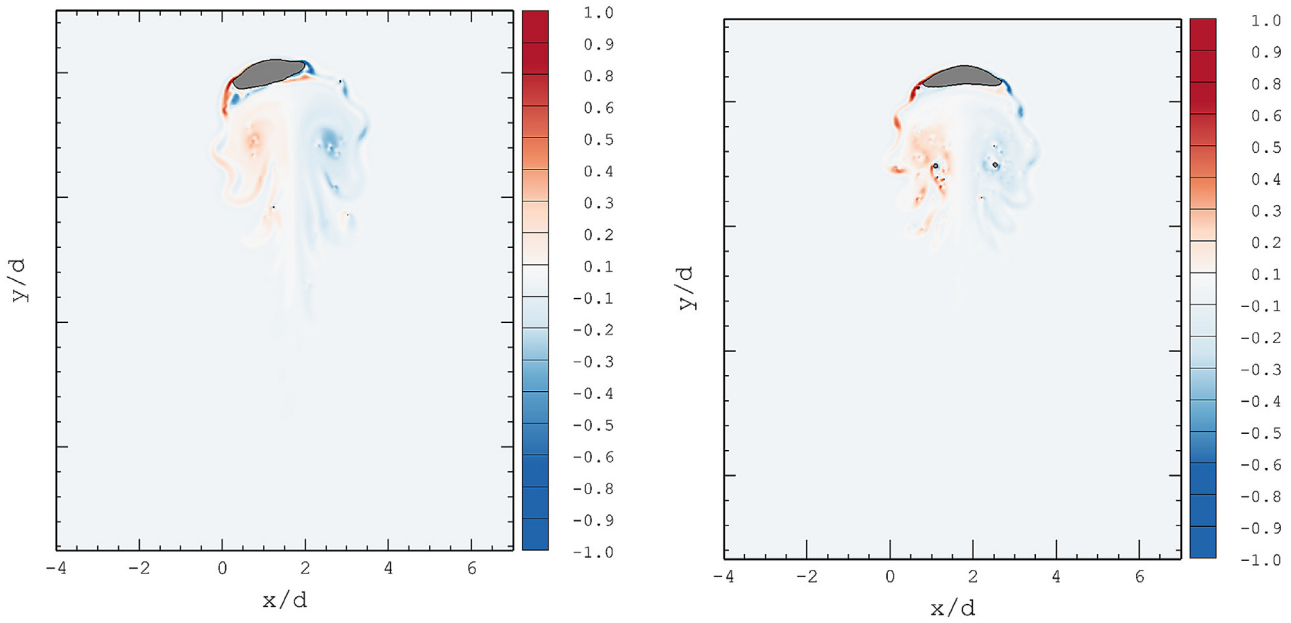

Fig. 16. Vorticity contours around the bubble at $Ar = 6,000$ (left panel) and $Ar = 11,000$ (right panel).

curved bubble interface. A periodic and alternate release of vortices of opposite vorticity is observed, where vorticity is generated at the bubble surface and evacuated in the flow through vortex shedding. The generated vortex is released when its maximum vorticity has been reached [55]. The generated vorticity is proportional to both the magnitude of the curvature of the bubble surface and the its velocity. Once the vortices are released their vorticity starts to decrease. As Ar increases further between $Ar = 6,000$ and $Ar = 11,000$, the wake structure changes from nonstationary to stationary. For $Ar = 6,000$ small instantaneous asymmetry of the near wake is observed, which causes slight transverse oscillation of the wake. For $Ar = 11,000$, the wake of the bubbles has recovered a stationary, symmetrical state and the bubble rises on a straight path. The simulation results for the evolution of the wake structure with Ar resemble the experimental observations in Roig et al. [54].

5. Concluding remarks

A mass-conserving FE-LBE model for simulating two-phase flow at high Reynolds numbers and large material property contrast has been proposed. The model is based on the conservative phase-field equation for interface capturing and the pressure-velocity formulation of lattice Boltzmann equation (LBE) for recovering the hydrodynamic properties. The Galerkin finite element method is applied to solving the conservative phase-field and discrete Boltzmann equations. The stability and accuracy of the model in capturing complex interface topologies are assessed through conducting several test cases for bubble rising problem in different flow regimes. The observed bubble shapes and the time evolution of the rising velocity and centroid of the bubble are consistent with previous experimental and numerical results. The model successfully predicts the complex dynamics of single bubble rising at a high Reynolds number. The evolution of the bubble shape as a function of Archimedes number and the observed Reynolds numbers of the rising bubble show a good agreement with the experimental results by Roig et al. [54]. The simulated wake dynamics, bubble path and shape oscillations in different regimes of oscillations agree well with experimental results. The proposed mass-conserving FE-LBE model improves a previous FE-LBE model [22] in terms of mass conservation. The FE-LBE model described here is a promising technique for simulation of a variety of multiphase flows at higher Reynolds numbers and complex geometries.

Declaration of Competing Interest

The authors declare that they have no known competing financial interests or personal relationships that could have appeared to influence the work reported in this paper.

CRediT authorship contribution statement

Lina Baroudi: Validation, Software, Writing - original draft. **Taehun Lee:** Conceptualization, Software, Supervision.

Acknowledgments

This work is supported by the US Department of Energy, Office of Nuclear Energy's Nuclear Energy University Programs. T.L. also acknowledges the partial support from the National Science Foundation under Award No. 1743794. L.B. and T.L. gratefully acknowledge the use of the CUNY High Performance Computing Clusters.

Appendix A. Fringe Zone

When a rising bubble is simulated using a computational domain with periodic boundary conditions in the ascent direction, the bubble can be affected by its own wake. The bubble wake can have an effect over a significant distance up to 50 times of the bubble diameter d. The nonzero velocities ahead of the bubble originating from its own wake can affect the shape and the dynamics of the bubble compare to a bubble rising in quiescent liquid. A fringe zone (shown in Fig. A.17) in front of the bubbles can be used to suppress the velocities generated by the bubble wake. Inside the fringe zone all the velocities are damped to zero. The fringe zone spans the entire horizontal plane and has a small height in the vertical direction, in our tests $0.25d$. The fringe zone moves with the bubble velocity U_t. The velocity inside the fringe zone are damped with the following forcing term

$$F_{fringe} = \frac{1}{\rho}\lambda(y)[U_0(y) - u(y)], \tag{A.1}$$

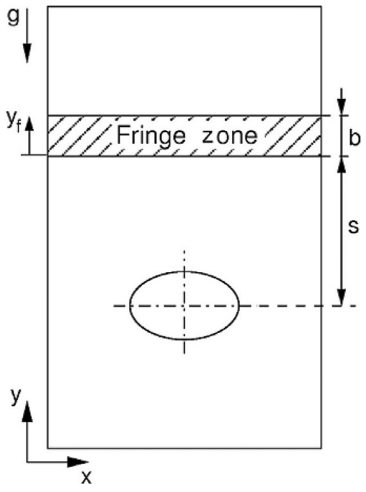

Fig. A.17. Position of the fringe zone. Adopted from Ref. [65].

toward a desired velocity U_0 (for our purpose $U_0 = 0$). The function $\lambda(y) = 0$ outside the fringe zone and takes the form of a smoothed step function inside the fringe zone as follows

$$\lambda(y) = \lambda_{\max}\left[S\left(\frac{y - y_{start}}{b_{start}}\right) - S\left(\frac{y - y_{end}}{b_{end}} + 1\right)\right], \tag{A.2}$$

where $\lambda_{\max}$ is the maximum amplification factor, y_{start} and y_{end} are the horizontal coordinate of the start and the end of the fringe zone, respectively, b_{start} and b_{end} are the widths over which the fringe function is ramped up from zero and ramped down to zero, respectively, and S is a step function given by

$$\begin{aligned} S(y_f) &= 0 \quad \text{if} \quad y_f \le 0 \\ S(y_f) &= \frac{1}{\left[1 + exp\left(\frac{1}{y_f - 1} + \frac{1}{y_f}\right)\right]} \quad \text{if} \quad 0 < y_f < 1 \\ S(y_f) &= 1 \quad \text{if} \quad y_f \ge 1. \end{aligned} \tag{A.3}$$

Based on numerous tests, the following parameters have been found suitable for the simulation of gas bubble with $d = 1$ rising in liquid: $s = 3d$, $b = 0.25d$, $\lambda_{\max} = 13$, $b_{start} = b_{end} = 0.05d$. The start and end coordinate of the fringe zone y_{start} and y_{end} are determined based on the position of the bubble center of mass.

References

[1] Tezduyar TE. Computation of moving boundaries and interfaces and stabilization parameters. Int J Num Methods Fluids 2003;43:555.
[2] Sethian JA, Smereka P. Level set methods for fluid interfaces. Ann Rev Fluid Mech 2003;35:341.
[3] Anderson DM, Fadden GBM, Wheeler AA. Diffuse-interface methods in fluid mechanics. Ann Rev Fluid Mech 1998;30:139.
[4] Liu C, Shen J. A phase field model for the mixture of two incompressible fluids and its approximation by a fourier-spectral method. Physica D 2003;179:211.
[5] Yue P, Feng JJ, Liu C, Shen J. A diffuse-interface method for simulating two-phase flows of complex fluids. J Fluid Mech 2004;515:293.
[6] Rowlinson JS, Widom B. Molecular theory of capillarity. Oxford: Clarendon Press; 1989.
[7] Allen SM, Cahn JW. Mechanisms of phase transformations within the miscibility gap of fe-rich fe-al alloys. Acta Metall 1976;24:425.
[8] Cahn JW, Hilliard JE. Free energy of a nonuniform system. I Interfacial free energy. J Chem Phys 1958;28:258.
[9] He XY, Luo L-S, 55. A priori derivation of the lattice Boltzmann equation. Phys Rev E 1997:R6333.
[10] Abe T. Derivation of the lattice Boltzmann method by means of the discrete ordinate method for the Boltzmann equation. J Comp Phys 1997;131:241.
[11] Lee T, Fischer PF. Eliminating parasitic currents in the lattice Boltzmann equation method for nonideal gases. Phys Rev E 2006;74:046709.
[12] Cao N, Chen S, Jin S, Martinez D. Physical symmetry and lattice symmetry in the lattice Boltzmann method. Phys Rev E 1997;55:R21.
[13] Namara GRM, Garcia AL, Alder BJ. Stabilization of thermal lattice Boltzmann models. J Stat Phys 1995;81:395.
[14] He X, Luo L-S, Dembo M. Some progress in lattice Boltzmann method. Part I Nonuniform mesh grids. J Comput Phys 1996;129:357.
[15] Mei R, Shyy W. On the finite difference-based lattice Boltzmann method in curvilinear coordinates. J Comput Phys 1998;143:426.
[16] Zhang R, Chen H, Qian YH, Chen S. Effective volumetric lattice Boltzmann scheme. Phys Rev E 2001;63:056705.
[17] Xi H, Peng G, Chou SH. Finite volume lattice Boltzmann method. Phys Rev E 1999;59:6202.
[18] Ubertini S, Bella G, Succi S. Unstructured lattice Boltzmann method: further development. Phys Rev E 2003;68:016701.
[19] Stiebler M, Tölke J, Krafczyk M. An upwind discretization scheme for the finite volume lattice Boltzmann method. Comput Fluids 2006;35:814.
[20] Lee T, Lin CL. Characteristic Galerkin method for discrete Boltzmann equation. J Comput Phys 2001;171:336.
[21] Lee T, Lin CL. An Eulerian description of the streaming process in the lattice Boltzmann equation. J Comput Phys 2003;171:445.
[22] Wardle KE, Lee T. Finite element lattice Boltzmann simulations of free surface flow in a concentric cylinder. Comput Math Appl 2013;65:230.
[23] Li Y, Boeuf EJL, Basu PK. Least-squares finite-element scheme for the lattice Boltzmann method on an unstructured mesh. Phys Rev E 2005;72:046711.
[24] Shi X, Lin J, Yu Z. Discontinuous Galerkin spectral element lattice Boltzmann method on triangular element. Int J Numer Meth Fluids 2003;42:1249.
[25] Min MS, Lee T. A spectral-element discontinuous Galerkin lattice-Boltzmann method for incompressible flows. J Comput Phys 2011;230:245.
[26] Zheng HW, Shu C, Chew YT. Lattice Boltzmann interface capturing method for incompressible flows. Phys Rev E 2005;72:056705.
[27] Zu YQ, He S. Phase-field-based lattice Boltzmann model for incompressible binary fluid systems with density and viscosity contrasts. Phys Rev E 2013;87:043301.
[28] Liang H, Shi BC, Guo ZL, Chai ZH. Phase-field-based multiple-relaxation-time lattice Boltzmann model for incompressible multiphase flows. Phys Rev E 2014;89:053320.
[29] Zheng L, Lee T, Guo Z, Rumschitzki D. Shrinkage of bubbles/drops in the lattice Boltzmann equation method for nonideal gases. Phys Rev E 2014;89:033302.
[30] Yue P, Zhou C, Feng JJ. Spontaneous shrinkage of drops and mass conservation in phase-field simulations. J Comput Phys 2007;223:1.
[31] Sun Y, Beckermann C. Sharp interface tracking using the phase-field equation. J Comput Phys 2007;220:626.
[32] Chiu P-H, Lin YT. A conservative phase field method for solving incompressible two-phase flows. J Comput Phys 2011;230:185.
[33] Geier M, Fakhari A, Lee T. Conservative phase-field lattice Boltzmann model for interface tracking equation. Phys Rev E 2015;91:063309.
[34] Kim SH, Pitsch H. On the lattice Boltzmann method for multiphase flows with large density ratios. J Comput Phys 2015;303:19.
[35] Comini G, Manzan M, Nonino C. Analysis of finite element schemes for convection-type problems. Int J Numer Methods Fluids 1995;20:443.
[36] Zienkiewicz OC, Codina R. A general algorithm for compressible and incompressible flow Part I. The split, characteristic-based scheme. Int J Numer Methods Fluids 1995;20:869.
[37] He X, Luo LS. Theory of the lattice Boltzmann method: from the Boltzmann equation to the lattice Boltzmann equation. Phys Rev E 1997;56:6811.
[38] Clift R, Grace JR, Weber M. Bubbles, drops, and particles. New York: Academic Press; 1978.
[39] Grace JR, Wairegi T, Nguyen TH. Shapes and velocities of single drops and bubbles moving freely through immiscible liquids. Trans Inst Chem Eng 1976;54:167.
[40] Chen L, Garimella SV, Reizes JA, Leonardi F. The development of a bubble rising in a viscous liquid. J Fluid Mech 1999;387:61.
[41] Zhang A, Guo Z, Wang Q, Xiong S. Three-dimensional numerical simulation of bubble rising in viscous liquids: a conservative phase-field lattice-Boltzmann study. Phys Fluids 2019;31:063106.
[42] Javadi K, Davoudian SH. Surface wettability effect on the rising of a bubble attached to a vertical wall. Int J Multiph Flow 2018;109:178.
[43] Hysing S, Turek S, Kuzmin D, Parolini N, Burman E, Ganesan S, Tobiska L. Quantitative benchmark computations of two-dimensional bubble dynamics. Internat J Numer Methods Fluids 2009;60:1259.
[44] Alnad S, Voigt A. Benchmark computations of diffuse interface models for two-dimensional bubble dynamics. Intl J Numer Meth Fluids 2012;69:747.
[45] Moore DW. The rise of a gas bubble in viscous liquid. J Fluid Mech 1959;6:113.
[46] Maxworthy T, Gnann C, Kurten M, Durst F. Experiments on the rise of air bubbles in clean viscous liquids. J Fluid Mech 1996;321:421.
[47] Hua J, Lou J. Numerical simulation of bubble rising in viscous liquid. J Comput Phys 2007;222:769.
[48] Magnaudet J, Eames I. The motion of high-Reynolds-number bubbles in inhomogeneous flows. Annu Rev Fluid Mech 2000;32:659.
[49] Ellingsen K, Risso F. On the rise of an ellipsoidal bubble in water: oscillatory paths and liquid-induced velocity. J Fluid Mech 2001;440:235.
[50] Mougin G, Magnaudet J. Path instability of a rising bubble. Phys Rev Lett 2002;88:014502.
[51] Prosperetti A. Bubbles. Phys Fluids 2004;16:1852.
[52] Kelley E, Wu M. Path instabilities of rising air bubbles in a hele-shaw cell. Phys Rev Lett 1997;79:1265.
[53] Bush JWM, Eames I. Fluid displacement by high Reynolds number bubble motion in a thin gap. Intl J Multiphase Flow 1998;24:411.
[54] Roig V, Roudet M, Risso F, Billete AM. Dynamics of a high-Reynolds-number bubble rising within a thin gap. J Fluid Mech 2012;707:444.

[55] Filella A, Ern P, Roig V. Oscillatory motion and wake of a bubble rising in a thin-gap cell. J Fluid Mech 2015;778:60.
[56] Piedra S, Ramos E, Herrera JR. Dynamics of two-dimensional bubbles. Phys Rev E 2015;91:063013.
[57] Wang X, Klaasen B, Degréve J, Blanpain B, Verhaeghe F. Experimental and numerical study of buoyancy-driven single bubble dynamics in a vertical hele-shaw cell. Phys Fluids 2014;26:123303.
[58] Wang X, Klaasen B, Degréve J, Mahulkar A, Heynderickx G, Reyniers M, Blanpain B, Verhaeghe F. Volume-of-fluid simulations of bubble dynamics in a vertical hele-shaw cell. Phys Fluids 2016;28:053304.
[59] Hashida M, Hayashi K, Tomiyama A. Rise velocities of single bubbles in a narrow channel between parallel flat plates. Int J Multiph Flow 2019;111:285.
[60] Scardovelli R, Zaleski S. Direct numerical simulation of free-surface and interfacial flow. Annu Rev Fluid Mech 1999;31:567.
[61] Sussman M. A parallelized, adaptive algorithm for multiphase flows in general geometries. Comput Struc 2005;83:435.
[62] Frank X, Funfschilling D, Midoux N, Li HZ. Bubbles in a viscous liquid: lattice Boltzmann simulation and experimental validation. J Fluid Mech 2006;546:113.
[63] Amaya-Bower L, Lee T. Single bubble rising dynamics for moderate Reynolds number using lattice boltzmann method. Comput Fluids 2010;39:1191.
[64] Antepara O, Balcázar N, Rigola J, Oliva A. Numerical study of rising bubbles with path instability using conservative level-set and adaptive mesh refinement. Comput Fluids 2019;187:83.
[65] Gaudlitz D, Adams NA. Numerical investigation of rising bubble wake and shape variations. Phys Fluids 2009;21:122102.
[66] Horowitz M, Williamson CHK. The effect of Reynolds number on the dynamics and wakes of freely rising or falling spheres. J Fluid Mech 2010;651:251.
[67] Schlatter P, Adams NA, Kleiser L. A windowing method for periodic inflow/outflow boundary treatment of non-periodic flows. J Comput Phys 2005;206:505.